DOI 10.1007/s11012-016-0553-5

Sediment transport and bedforms: a numerical study of two-phase viscous shear flow

F. Charru · J. Bouteloup · T. Bonometti · L. Lacaze

Abstract After a quick overview of recent research on sediment transport by shear flow and ripple and dune formation, original numerical results are presented from two-phase flow modelling of the interaction between a viscous flow and a bed of particles. Good agreement is found with previous experiments or numerical simulation, notably for the particle flux and velocity profiles within the moving layer. Bed instability is also found, giving rise to ripples whose characteristics are discussed.

Keywords Sediment transport · Ripples and dunes · Two-phase numerical simulation

1 Introduction

For more than a century, the question of sediment transport by fluid flows, and the growth and migration of sand ripples and dunes, have stimulated numerous field observations, laboratory experiments, theoretical analyses and more recently numerical simulations. The issues concern many fields of human activity, e.g. agriculture, waterways and maritime facilities, water processing and effluent treatment, and industries managing granular materials; at larger scale, the issue is the understanding of geomorphology on Earth and distant planets with the recent availability of satellite observations.

In spite of the importance of the above issues, both scientific and economic, sediment transport still escapes from clear understanding and efficient predictive laws. The first part of the present paper offers a quick overview of the state of the art, restricted to viscous laminar flow (Sect. 2). The second part provides original results from numerical simulations of two-phase viscous shear flow. Numerical simulation now appears, indeed, as a powerful and reliable tool for the investigation of the physics of particle-laden flows. The modelling and numerical method are presented first (Sect. 3), and then results for particle transport (Sect. 4) and ripple formation (Sect. 5). These results provide new insight and help the interpretation of viscous flow experiments, and may be relevant in any situation where the bedload layer lies within the viscous sublayer of turbulent boundary layers.

2 Overview

2.1 Particle transport under uniform and steady flow over a flat bed

Shear stress threshold for the onset of sediment transport. Let's consider an horizontal bed of particles

F. Charru (✉) · J. Bouteloup · T. Bonometti · L. Lacaze
IMFT, Université de Toulouse, CNRS, INPT, UPS, Toulouse, France
e-mail: francois.charru@imft.fr

sheared by a fluid flow, either air or water or any liquid. Basic observation shows that for small fluid shear stress acting on the bed, τ_b, the particles stay at rest. As the shear stress is increased, some prominent particles, more exposed to the fluid flow, are set in motion; however, after having travelled over some distance, they fall in small troughs of the disordered bed, and their motion stops. For τ_b beyond some threshold τ_t, a steady particle flow rate eventually sets in [9]. The scaling law for τ_b can be obtained from the balance of the forces acting on one particle (here assumed to be spherical or nearly spherical with diameter d): the hydrodynamic force, of order $\tau_b d^2$, must scale with the immersed weight of the particle, of order $(\rho_p - \rho)gd^3$, where g is the acceleration of gravity and ρ_p and ρ are the particle and fluid densities, respectively. An important dimensionless number arises, the Shields number, as the ratio of the hydrodynamic and gravity forces:

$$\theta = \frac{\tau_b}{(\rho_p - \rho)gd}. \tag{1}$$

At threshold, the Shields number takes the typical value $\theta_t \approx 0.1$. This threshold, which can be viewed as an effective friction coefficient, however depends on the viscous or inertial nature of the flow at the particle scale, i.e. on the particle Reynolds number

$$Re_p = \frac{\rho u_* d}{\mu} \tag{2}$$

where μ is the viscosity and u_* a characteristic fluid velocity [32]. For viscous flow ($Re_p < 5$ with $u_* = \gamma d$ and γ the shear rate), θ_t is close to 0.12. For $Re_p \gtrsim 5$, θ_t first decreases down to 0.03 and then increases to the constant value 0.05. In the latter 'rough regime', the grains have size larger than the viscous layer and emerge in the turbulent flow where velocity fluctuations are of the order of the friction velocity $u_* = (\tau_b/\rho)^{1/2}$. The precise value of the threshold may however be defined in several ways and depends on the initial preparation of the bed, leading to some scatter in the literature. Hence, the onset of particle motion may rather correspond to a continuous transition from creeping to granular flow, as shown by [19].

Surface density and velocity of the moving particles Beyond the threshold θ_t, the particle flow rate q (the volume of particles crossing a transverse section of the flow per unit time and flow width) increases with the bed shear stress τ_b. Considerable work has been devoted to the derivation of semi-empirical laws $q(\tau_b)$. The physical meaning of these laws can be understood on considering that

$$q = \frac{\pi d^3}{6} n\, U_p \tag{3}$$

where n is the particle surface density (number of moving particles per unit horizontal area) and U_p is the particle speed averaged over the moving particles. Following [3], the dimensionless surface density nd^2 can be shown to be proportional to $\theta - \theta_t$. This result follows from the idea that across the moving layer, the shear stress τ_f transmitted by the fluid decreases from τ_b to τ_t at its lower boundary (on the non-moving bed), whereas that transmitted by the grains, $\tau_p = \tau_b - \tau_f$, increases and follows the Coulomb friction law. The same result can be obtained from a different argument based on an erosion-deposition model [24]. The same argument holds for viscous flow, where experiments [9, 19] show that

$$nd^2 = 0.47\,(\theta - \theta_t), \qquad \theta_t = 0.12. \tag{4}$$

The speed U_p results from a balance between the force exerted by the flow and the resistance of the bed, and was shown by [4] to be proportional to $u_* - u_{*t}$ where u_{*t} is some minimum particle speed at threshold. Bagnold's analysis was confirmed by experiments by [16] and [24] for turbulent flow. For laminar viscous flow, experiments showed $U_p = 0.1\gamma d$ [9], which, on the basis of a momentum balance similar to that of [4], can be written as

$$\frac{U_p}{V_S} = 1.8\,\theta, \tag{5}$$

where

$$V_S = \frac{(\rho_p - \rho)gd^2}{18\mu} \tag{6}$$

is the Stokes settling velocity.

Particle flux Combining the above laws for the surface density n and the particle speed U_p provides the quadratic dependence

$$\frac{q}{V_S d} = a\theta(\theta - \theta_t), \qquad a = 0.44, \qquad \theta_t = 0.12. \tag{7}$$

Note that (4) and (5) were established for $\theta < 0.7$ where the thickness of the moving layer remains smaller than three particle diameters. Note also that the different scaling with the shear stress of the particle flow rate for turbulent and laminar flow, $q \propto \tau^{3/2}$ and $q \propto \tau^2$, respectively, arises not from the surface density n, which is linear for both flows, but from the particle velocity which scale with $u_* = (\tau/\rho)^{1/2}$ for the former and $u_* = \tau d/\mu$ for the latter.

Inside the moving layer Just above threshold, only a monolayer of particles moves. However, for $\theta \gtrsim 2\theta_t$, the thickness of the moving layer increases and the question arises of the internal structure of the moving layer. This question has been addressed theoretically by [3] and [25]. According to Bagnold's model, the momentum transfer across the moving layer is the sum of a fluid shear stress and a particle shear stress, each proportional to the local shear rate and an effective viscosity. The resulting concentration profile however decreases slowly with height so that the particle flux diverges logarithmically. [25] developed a viscous resuspension theory, for particles without inertia, based on the idea that within the moving layer, the settling flux due to gravity is counterbalanced by a diffusion flux proportional to the local particle concentration gradient. This theory, which does not account for any threshold shear stress, predicts [8]

$$\frac{q}{V_S d} = 7.5\,\theta^3. \tag{8}$$

These theories have been assessed experimentally in viscous flow by [26], by matching the optical index of the fluid and the particles and illuminating a few dyed particles with a laser sheet. The velocity profiles for both the fluid and particles appeared to be parabolic. A model was also proposed, based on Bagnold's ideas with the simplification of uniform friction coefficient $\tan\alpha$ (where α is the friction angle), effective viscosity μ_{eff} and particle concentration ϕ, and the neglect of particle inertia. This model allows the measured velocity profiles for the fluid, $u_f(y)$, and the particles, $u_p(y)$, to fall on the unique curve

$$\frac{u_p}{V_S} = \frac{u_f}{V_S} = \frac{9\,\phi\tan\alpha}{\mu_{\text{eff}}/\mu}\left(\frac{y+h_b}{d}\right)^2 \tag{9}$$

where y is measured from the bed surface at rest, and $\tan\alpha = 0.75$, $\mu_{\text{eff}}/\mu = 2.45$ and $\phi = 0.27$. The depth h_b where the velocity vanishes, and the total thickness $h_b + h_m$ of the moving layer (see Fig. 1), increase linearly with shear stress, as

$$\frac{h_b}{d} = \frac{\theta}{\phi_0\tan\alpha}, \qquad \frac{h_m + h_b}{d} = \frac{\theta}{\phi\tan\alpha} \tag{10}$$

where $\phi_0 = 0.6$ is the particle concentration in the bed at rest. The internal structure of the moving layer has also been investigated numerically, notably by [27], using a two-phase flow modelling, and by [15] and [23], see Sect. 4.

2.2 Ripples and dunes

The distinction between ripples and dunes. A major feature of the flow over an erodible bed is that an initially flat bed does not remain flat: small ripples grow, with wavelength of a few centimeters. The origin of the instability is fluid inertia, which compete with the stabilizing effect of gravity and granular relaxation effects for the wavelength selection, see the review by [10]. As their amplitude grows, ripples quickly develop a triangular shape with gentle upstream slope and steep downstream slip face (with slope of about 30°) where the shear stress is small. These finite-amplitude (nonlinear) ripples propagate with velocity

$$c = \frac{q_{\text{crest}}}{H}, \tag{11}$$

proportional to the particle flux at the crest and inversely proportional to their height H. This important law, which arises from mass conservation on the slip face, implies that small ripples travel faster than larger ones and merge with them, which induces a coalescence process. The characteristic size of the resulting bedforms thus increases with time (or space) whereas their velocity slows down. The nonlinear

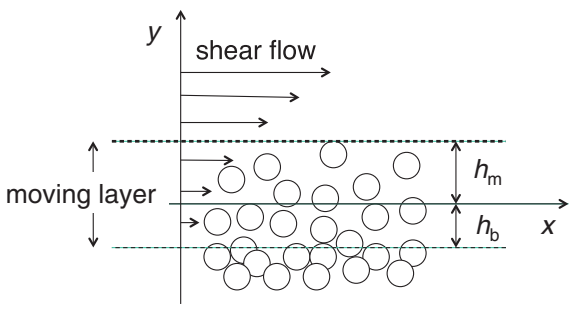

Fig. 1 Sketch of the moving particles layer, and definition of the thicknesses h_b and h_m

coarsening of the pattern eventually stops when its size becomes comparable with an external geometrical length, typically the flow depth for rivers [17, 28]. These bedforms, with typical wavenumber $kH \approx 1$, are referred to as 'dunes'. In shallow flows however (i.e. for flow depth comparable with the ripple length, i.e. of a few centimeters), dunes may appear as the result of a primary longwave instability, through the coupling with the deformable upper free surface [13]: the growth rate of this 'dune mode' may indeed be comparable to that of the 'ripple mode'.

For unidirectional flow, the dunes remain two-dimensional (i.e. more or less invariant in the transverse direction), but three-dimensional patterns often develop. This is notably the case for aeolian dunes when the direction of the wind changes, or when the dune migrates over a non-erodible ground (e.g. large pebbles) giving rise to crescentic shapes known as barchan dunes. Under water, dunes also exhibit a large variety of patterns which have been reviewed by [5] for the coastal environment and [29] for rivers. Note that extreme events, such as storms or floods, transport huge quantities of sediment and may completely reset the spatial distribution of bedforms.

In conclusion, it can be said that important questions remain unclear, even for laminar flow: effective boundary conditions for the calculation of the fluid flow [12], particle transport close to threshold, diffusive action of gravity, relaxation effects. Numerical simulation of the two-phase flow taking place within the bedload layer now appears as a reliable tool for the investigation of these questions. The first step of such simulations is to recover the robust results gained from experiments. This is the aim of the following part of this paper.

3 Description of the Euler–Lagrange method

The numerical strategy adopted here permits to capture the formation of multiple ripples and dunes without the need of describing the fields around each grain (as done in [22]). It consists in using an Euler–Lagrange method with which the flow is solved on an Eulerian grid, with mesh size slightly larger than the grain size, while individual particles are tracked in a Lagrangian way using Discrete Element Method to account for grain–grain interactions.

3.1 Calculation of the fluid flow

In problems dealing with bedload transport, the local volume fraction of the granular phase $\phi = 1 - \varepsilon$ can be large, namely of the order of the maximum random packing inside the bed (ε is the fluid-phase volume fraction). In order to take into account the presence of the dense granular phase in the fluid equations, one may apply a local volume filtering to the Navier–Stokes equations, as done by [1] in the context of fluidized beds. The reader is also referred to [7] for a detailed derivation of the equations. The continuity and momentum equations then read

$$\frac{\partial \varepsilon}{\partial t} + \nabla \cdot (\varepsilon \mathbf{u}) = 0, \tag{12}$$

$$\rho\varepsilon\left(\frac{\partial \mathbf{u}}{\partial t} + \mathbf{u}\nabla\mathbf{u}\right) = \nabla \cdot \mathbf{S} - \mathbf{f} + \rho\varepsilon\mathbf{g}, \tag{13}$$

where ε, ρ, $\mathbf{u}$ are the fluid-phase volume fraction, density and velocity, respectively, $\mathbf{S}$ is the volume-filtered stress tensor, $\mathbf{f}$ is the interphase exchange term and $\mathbf{g}$ is the acceleration vector due to gravity.

The volume-filtered stress tensor is here modeled as

$$\mathbf{S} = -\varepsilon p\mathbf{I} + \mu\varepsilon^{-2.8}\left[\nabla\mathbf{u}_m + (\nabla\mathbf{u}_m)^T\right], \tag{14}$$

where p and μ are the fluid-phase pressure and dynamic viscosity, respectively, and $\mathbf{u}_m = \varepsilon\mathbf{u} + \phi\mathbf{v}$ is the mixture velocity which depends on the fluid- and granular-phase velocities $\mathbf{u}$ and $\mathbf{v}$, respectively. Following [27] and [11], the present choice of using $\mathbf{u}_m$ in (14) instead of $\mathbf{u}$ allows the trace of $\mathbf{S}$ to be zero, as is the case for the viscous stress tensor of an incompressible fluid. Note here that the *effective* viscosity in $\mathbf{S}$ strongly depends on ε via the prefactor $\varepsilon^{-2.8}$ in order to take into account the effect of the local grain concentration [18]. With the present choice, the effective viscosity is roughly increased by an order of magnitude from regions far from the granular bed to those inside the bed. In practice, ε, $\mathbf{f}$ and the term $\phi\mathbf{v}$ used in the calculation of $\mathbf{S}$ are computed using Lagrangian quantities. The specific calculation of these terms is given in Sect. 3.3.

The fluid solver used here is the JADIM code developed at IMFT. Briefly, this code is a finite-volume method solving the three-dimensional, time-dependent Navier–Stokes equations (13) is solved on a staggered grid using second-order central differences for the spatial discretization and a third-order Runge–

Kutta/Crank–Nicolson method for the temporal discretization. The incompressibility condition is satisfied using a projection technique. The overall algorithm is second-order accurate in space and time. More details about the numerical procedure, without grains ($\phi = 0$, $\varepsilon = 1$), can be found in [6]. Domain decomposition and Message-Passing-Interface (MPI) parallelization is performed to facilitate the simulation of large number of computational cells.

3.2 Calculation of the grains motion

The grains motion is computed in a Lagrangian way. For each spherical particle of diameter d, mass m_p, linear and angular velocity $\mathbf{u}_p$ and $\boldsymbol{\omega}_p$, respectively, we solve Newton's equations for the linear and angular momentum,

$$m_p \frac{d\mathbf{u}_p}{dt} = m_p \mathbf{g} + \mathbf{F}_c + \mathbf{F}_w + \mathbf{F}_h, \tag{15}$$

$$\mathbf{I}_p \frac{d\boldsymbol{\omega}_p}{dt} = \boldsymbol{\Gamma}_c + \boldsymbol{\Gamma}_w + \boldsymbol{\Gamma}_h, \tag{16}$$

where $\mathbf{I}_p = \frac{1}{10} m_p d^2\ \mathbf{I}$ is the isotropic inertia matrix, $\mathbf{F}_c$ and $\mathbf{F}_w$ are the inter-particle and wall-particle contact forces, respectively, $\mathbf{F}_h$ is the hydrodynamic force exerted on the particle by the surrounding fluid and $\boldsymbol{\Gamma}_c$, $\boldsymbol{\Gamma}_w$ and $\boldsymbol{\Gamma}_h$ are the corresponding torques. In the present approach, the size of the particles relative to the characteristic scales of the flow is assumed to be small enough so the fluid can be considered uniform at the grain scale, so that we set from now on $\boldsymbol{\Gamma}_h = 0$.

The modeling of inter-particle and wall-particle interactions is done via a soft-sphere approach [14], also denoted discrete element method (DEM). This approach is based on modeling the deformation of real particles during contact by an overlap between computed non-deformable particles. The overlap is then used to compute the normal and tangential contact forces, using here a linear mass-spring system and a Coulomb type threshold for the tangential component, in order to account for solid sliding. The description and validation of the present DEM used to compute $\mathbf{F}_c$, $\mathbf{F}_w$, $\boldsymbol{\Gamma}_c$ and $\boldsymbol{\Gamma}_w$, are given in [20] and [21], respectively, to which we refer to for more details. It is worth noting however, that the input physical parameters for the present soft-sphere approach are the coefficient of normal restitution e_n, contact time t_c and the local friction coefficient μ_c which will be specified later.

Following [7], the modeling of the hydrodynamic force $\mathbf{F}_h$ exerted on the particle by the surrounding fluid reads

$$\mathbf{F}_h \approx \mathcal{V}_p \nabla \cdot \mathbf{S} + \mathbf{F}_d, \tag{17}$$

where $\mathcal{V}_p$ is the volume of the particle, $\mathbf{S}$ is the volume-filtered stress tensor and $\mathbf{F}_d$ is the drag force. The first term on the right-hand side of (17), referred to as the generalized buoyancy force [1], accounts for the volume-filtered fluid pressure gradient force and viscous stress at the location of the particle (see Eq. 14), while the second term includes the local drag acting on the particle. Other hydrodynamic contributions will be ignored here, notably the viscous Basset force and lubrication force between the particles, as well as the inertial lift and added mass forces. While such forces are expected to play a major role in flows where sediment is transported as a suspension, it is likely that their contribution is somewhat smaller or even marginal in the case of viscous flows where the only type of sediment transport is bedload.

The drag force $\mathbf{F}_d$ is computed using [30]'s correlation derived from particle-resolved numerical simulations of flows around arbitrary arrays of spheres, namely

$$\mathbf{F}_d = 3\pi\mu d\varepsilon(\mathbf{u} - \mathbf{u}_p)\mathcal{F}(\varepsilon, Re_m), \tag{18}$$

where $\mathcal{F}$ is a drag coefficient which depends on the fluid volume fraction ε and a local particle Reynolds number Re_m defined as $Re_m = \rho\varepsilon|\mathbf{u} - \mathbf{u}_p|d/\mu$. Note that Re_p defined in (1) and Re_m are equivalent if one takes $u_* = \varepsilon|\mathbf{u} - \mathbf{u}_p|$. The drag coefficient $\mathcal{F}$ can be written as $\mathcal{F} = \mathcal{F}_0 + \mathcal{F}_1 + \mathcal{F}_2$ where [30]

$$\begin{aligned}
\mathcal{F}_0(\varepsilon, Re_m) &= \frac{1 + 0.15 Re_m^{0.687}}{\varepsilon^2}, \\
\mathcal{F}_1(\varepsilon) &= \frac{5.81(1-\varepsilon)}{\varepsilon^2} + \frac{0.48(1-\varepsilon)^{1/3}}{\varepsilon^3}, \\
\mathcal{F}_2(\varepsilon, Re_m) &= \varepsilon(1-\varepsilon)^3 \left(0.95 + \frac{0.61(1-\varepsilon)^3}{\varepsilon^2}\right) Re_m.
\end{aligned} \tag{19}$$

3.3 Interphase coupling

The influence of the fluid phase on the granular phase in (15) comes from the term $\mathbf{F}_h$ while that of the granular phase on the fluid phase in (13) appears via

$\varepsilon = 1 - \phi$, $\mathbf{f}$ and $\phi\mathbf{v}$ used in the calculation of $\mathbf{S}$. These latter terms are first computed at the location of each particle, and are then transferred to the Eulerian grid. The interpolation of the fluid variables to the particle location are done using a second order interpolation scheme, while the extrapolation of the particle data to the Eulerian grid is done using a volume filtering operation. More precisely, ϕ is computed as

$$\phi = \frac{1}{\mathcal{V}_c} \sum_{p=1}^{\tilde{N}_p} \alpha_p \mathcal{V}_p, \tag{20}$$

where $\tilde{N}_p$ is the number of particles located in a limited region surrounding the Eulerian grid cell, $\mathcal{V}_c$ and $\mathcal{V}_p$ are the volume of the computational cell and that of the pth-particle, respectively. $\mathbf{f}$ and $\phi\mathbf{v}$ are computed in a similar manner by replacing $\mathcal{V}_p$ in (20) by $\mathbf{F}_h$ and $\mathcal{V}_p\mathbf{u}_p$, respectively. The coefficient α_p is a weighting factor using a kernel function K which monotonically decreases with distance from the particle, namely [31]

$$\alpha_p = \frac{K(|\mathbf{x}_p - \mathbf{x}_c|)}{\sum_{l=1}^{N_c} K(|\mathbf{x}_p - \mathbf{x}_l|)}, \tag{21}$$

$$K(\zeta) = \begin{cases} [1 - (\zeta/\sigma)^2]^4, & \text{si} |\zeta/\sigma| < 1 \\ 0, & \text{si} |\zeta/\sigma| \geq 1 \end{cases} \tag{22}$$

In (21)–(22), $\mathbf{x}_c$ is the location of the grid cell center, $\mathbf{x}_p$ is the particle location, N_c is the number of Eulerian grid cells located in a limited region surrounding the particle and σ is the bandwidth of the kernel function typically taken as $\sigma = 2\mathcal{V}_c^{1/3}$. With the present choice, the effect of the particle is typically spread out over one or two neighboring cells in all directions.

4 Particle motion under a steady flow

4.1 Physical and numerical setup

We now turn to the specific case of the shearing of a bed of particles by Couette flow. As mentioned earlier, the bedload transport can be characterized by three dimensionless parameters, namely the Shields number, the particle Reynolds number and the density ratio. Taking as characteristic fluid shear stress and velocity $\tau_b = \mu\gamma$ and $u_* = \gamma d$, respectively, γ being the mean fluid shear rate, the dimensionless parameters defined in (1) and (2) can be rewritten as

$$\theta = \frac{\mu\gamma}{(\rho_p - \rho)gd}, \qquad Re_p = \frac{\rho\gamma d^2}{\mu}. \tag{23}$$

The numerical results will be compared with recent experiments [2, 9, 26], numerical simulations [15, 23] and theoretical analyses [8, 27], which provide detailed descriptions of the fluid and granular flow inside the bed. In particular, the above numerical simulations were done using an immersed-boundary-method which solves the flow around each particle, and hence can be considered as a reference relative to the present approach where the flow is solved at a scale larger than the grain diameter. It is also worth noting that bedload transport is driven by a laminar Couette flow in [8, 9, 15, 26] while it is driven by an imposed pressure gradient (Poiseuille) flow in [2, 23, 27].

In the present section, we set $Re_p = 0.5$ and $\rho_p/\rho = 4$, as [15] in their numerical simulations, and vary θ in the range $0 \leq \theta \leq 0.7$. The physical input parameters for the DEM, namely the collision time, the coefficient of normal restitution, and the friction coefficient, are set to $\gamma t_c = 2 \times 10^{-4}$, $e_n = 0.8$ and $\mu_c = 0.4$, respectively. Actually, [15] and [23] have shown that varying e_n and μ_c does not change the results significantly.

A sketch of the flow is depicted in Fig. 2, showing the bed of particles (randomly placed at the initial time), and the pure fluid sheared by the upper wall with velocity U_0 in the x-direction. The particles in contact with the lower wall are fixed. A Cartesian domain of size $L_x = 20d$, $L_y = 20d$ and $L_z = 10d$ along the streamwise, vertical and spanwise directions, respectively, is used. The spatial resolution is uniform, with $\Delta x = \Delta y = \Delta z = 2d$, corresponding to a number of cells $N_x = 10$, $N_y = 10$ and $N_z = 5$. No-slip boundary conditions are imposed along the bottom and top walls, while periodic boundary conditions are used in the x- and z-directions. Gravity is oriented towards the negative y-direction. The initial height of the bed is $10d$. At initial time, a linear velocity profile with shear rate γ is imposed in the liquid with zero velocity just above the granular bed, and the particles are at rest.

Note that the size of the computational domain is relatively small, in particular in the streamwise direction. This was done in order to prevent any bed instability (such as ripples or dunes) and keep the bed flat. An example of ripple formation in a larger domain is presented in Sect. 5.

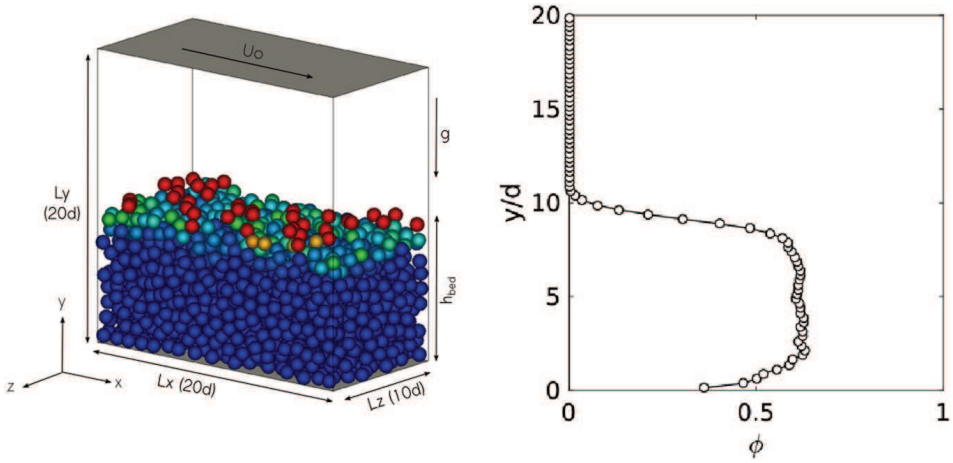

Fig. 2 (Color online) (*a*) Flow geometry, coordinate system, and instantaneous streamwise particle velocity for $\rho_p/\rho = 4$, $Re_p = 0.5$, $\theta = 0.35$: *blue*, $u_p = 0$; *red*, $u_p \approx 0.5\gamma d$). (*b*) vertical profile of the solid volume fraction ϕ, horizontally averaged, when the steady-state is reached

4.2 Particle flow rate and height of the granular bed

A sample of the time evolution of the particle flow rate $q(t)$ and the mean height of the granular bed $h(t)$ are presented in Fig. 3 for $\theta = 0.35$. The mean particle flow rate, that is the volumetric flow rate per unit width (in m^2/s), is computed as

$$q(t) = \frac{1}{L_x L_z} \sum_{p=1}^{N_p} \mathcal{V}_p u_p(t) \tag{24}$$

with $\mathcal{V}_p$ the volume of the p-th particle and N_p the total number of particles (excluding those which are fixed at the bottom wall).

The bed height is computed as the horizontal average of the vertical position of the topmost particles in each cell:

$$h(t) = \frac{1}{N_x N_z} \left(\sum_{i=1}^{N_x N_z} \max_{p \in i} (y_p(t)) \right) + 0.5d \tag{25}$$

with y_p the vertical location of the p-th particle's center.

As shown in Fig. 3, the particle flow rate increases during a transient time of about $\gamma t \approx 200$, and then saturates to a constant value, with fluctuations of about 20 % (which would be smaller if averaged over a larger domain). The bed height $h(t)$, initially of $9.5d$, increases similarly of about $0.2d$, on the same time scale, corresponding to the decompaction of the moving layer. Note that the transient time $200/\gamma$ corresponds to $(200/18\theta)d/V_S \approx 32\, d/V_S$ where d/V_S is a characteristic settling time.

4.3 Fluid and particle velocity profiles

We now turn to the streamwise velocity profiles along the wall-normal direction. For the granular velocity profile, the y-direction is decomposed in horizontal layers of thickness $\Delta h = d/4$ where space-averaging is performed [23]. Introducing an indicator function of the j-th layer

$$\delta^j(y) = \begin{cases} 1 & \text{if} \quad (\mathrm{j}-1)\,\Delta\mathrm{h} \le \mathrm{y} < \mathrm{j}\,\Delta\mathrm{h}, \\ 0 & \text{otherwise}, \end{cases} \tag{26}$$

the instantaneous number of particles in the j-th layer at time t_m is computed as

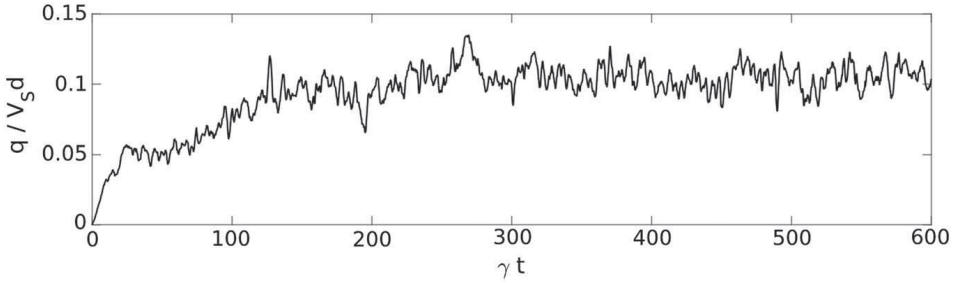

Fig. 3 Sample of the time evolution of the particle flow rate

$$\langle n_p \rangle_{xz}^{j}(t_m) = \sum_{p=1}^{N_p} \delta^j(y_p(t_m)) \tag{27}$$

where y_p is the vertical location of the p-th particle's center and N_p is the total number of particles. Integration over time then reads

$$\langle n_p \rangle_{xzt}^{j} = \sum_{m=1}^{N_t} \langle n_p \rangle_{xz}^{j}(t_m), \tag{28}$$

with N_t being the number of time samples used in the averaging process. the granular velocity profile is computed in a similar manner as

$$\langle u_p \rangle_{xzt}^{j} = \frac{1}{\langle n_p \rangle_{xzt}^{j}} \sum_{m=1}^{N_t} \sum_{p=1}^{N_p} \delta^j(y_p(t_m)) u_p(t_m). \tag{29}$$

All quantities were time-averaged using at least $N_t = 100$ time samples and a time duration of $\gamma t = 200$.

Figure 4a displays particle and fluid velocity profiles for $\theta = 0.35$. The slip velocity between the fluid and the particles clearly appears, with magnitude of about $0.2\,u_p$ (note that the spatial resolution in the fluid, $\Delta y = 2d$, is much coarser than that for the particles, which is d / 4).

Figure 4b displays particle velocity profiles for six Shields numbers in the range $0.2 \leq \theta \leq 0.5$. In order to assess the present calculations with the measurements of [26] and equation (9), the velocity profiles are shifted vertically by h_b/d (see Fig. 1) according to (10), with the same values for the solid volume fraction $\phi_0 = 0.6$ and the effective friction coefficient $\tan\alpha = 0.75$. The agreement appears remarkable. In this Figure, the numerical results of [15] are also plotted, showing again excellent agreement.

4.4 Particle flux

We now consider the particle flow rate and its variation with the Shields number. As mentioned earlier, [9] observed that close to the threshold Shields number, where only the uppermost grains move, the particle flow rate increases quadratically with θ, according to Eq. (7). For higher Shields numbers, $\theta \gtrsim 2\theta_t$ where the thickness of the mobile layer is larger than one diameter, the particle flow rate rather increases as θ^3, see (8) and [23, 27].

Results from the present Couette flow simulations are displayed in Fig. 5 for $\theta < 0.7$, together with experimental data by [9] and numerical points by [15]. It appears that all data points fall close to the cubic law (8), provided that a threshold $\theta_t = 0.14$ is introduced in this law, as done by [8]. However, close to threshold (see the close-up view in the inset), the parabolic law (7) fits the data much better, as expected since there the thickness of the moving layer is small, of the order of one single particle diameter. Recall that, unlike [15] whose method involves the full description of the flow around each particle, our numerical model does not solve the flow at the particle scale. Thus, it is *a priori*

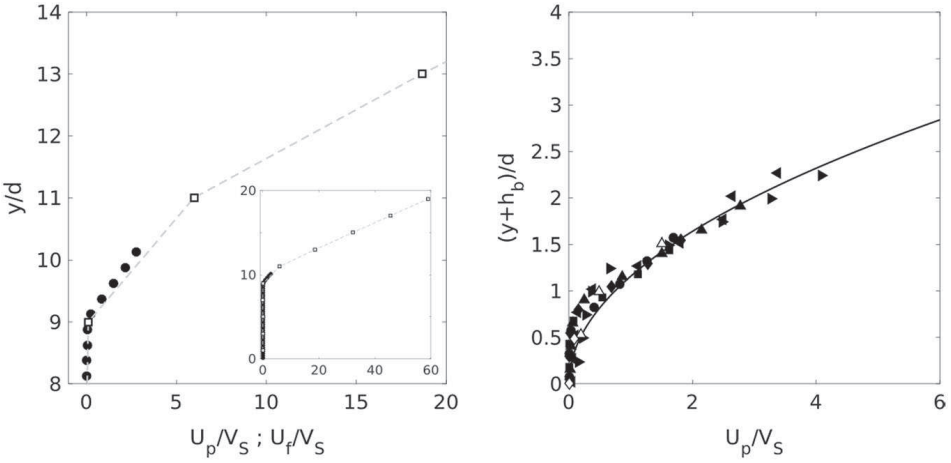

Fig. 4 (**a**) Vertical profile of the streamwise fluid velocity u_f/V_S (*open square*) and the particle velocity u_p/V_S (*filled circle*) for $\theta = 0.35$, in the vicinity of the mobile layer. *Inset* larger view over the whole computational domain. (**b**) Particle velocity scaled according to (9), for Shields numbers $\theta = 0.20$ (*filled circle*), $\theta = 0.25$ (*filled square*), $\theta = 0.30$ (*filled daimond*), $\theta = 0.35$ (*filled triangle*), $\theta = 0.40$ (*filled left triangle*) and $\theta = 0.50$ (*filled right triangle*). *Solid line* Eq. (9) from [26]. *Open symbols*: [15] for $\theta = 0.20$ (*open daimond*), $\theta = 0.42$ (*open triangle*)

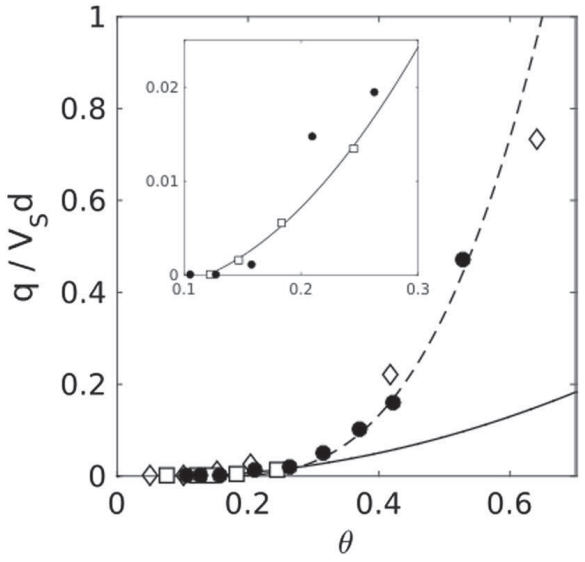

Fig. 5 Dimensionless flow rate $q/V_S d$ versus Shields number θ for Couette flow: present simulations (*filled circle*), [15] (*open daimond*), [9] (*square*). *Solid line* parabolic law (7); *dashed line* cubic law (8) with $\theta_t = 0.14$. *Inset* close-up view near threshold

not well suited to capture the subtle physical processes at work near incipient motion. With this in mind, the observed agreement is in fact remarkable.

5 Ripple formation

We now assess the ability of the numerical code to reproduce the instability of the flat bed and the growth of ripples. The main difference with the simulations of the previous section lies in the much larger size of the numerical domain along the streamwise direction, which is now $L_x = 1000\,d$ instead of $20\,d$. The other (minor) difference is that the flow is initially at rest instead of being defined by a linear velocity profile. The dimensionless numbers are set to $Re_p = 7.5$, $\rho_p/\rho = 2.5$ and $\theta = 0.4$, while the physical input parameters for the DEM remain unchanged.

Figure 6 displays the bed position (computed from the vertical position of the uppermost particles), at initial time and $\gamma t = 6000$. It appears that the bed does not remain flat, and that triangular ripples appear. The largest ripples have wavelength of about $200\,d$ but smaller ones can be seen too, together with small ripples on the upstream face of larger ones.

The coarsening process arises from the fact that, as discussed in the Introduction Section, the velocity c of finite-amplitude ripples is inversely proportional to their height, $c = q_{\text{crest}}/H$ (11), where q_{crest} is the particle flux at the crest. Let us discuss this relation. The particle flux along the bed is shown in Fig. 7: this flux experiences large variations, being nearly zero at the dune foot and increasing strongly towards the crests. The mean value is about $0.5\,V_S d$, much larger than that on flat bed (about $0.2\,V_S d$ for the same Shields number, see Fig. 5). Thus, a rippled bed transports many more particles than a flat one, with flux at the crest being larger by one order of magnitude. From spatio-temporal diagrams (not shown), the velocity of large ripples can be estimated as $c \approx 0.4\,\gamma d$ for $\theta = 0.4$; this velocity is smaller than the velocity of the fastest particles on the flat bed (of about $0.6\,\gamma d$ from Fig. 4) but larger than the mean velocity. The ripple height H may then be calculated from (11), giving, for the highest ripple, $H \approx 2.5 V_S d/0.4\gamma d \approx (0.35/\theta)d \approx 0.9\,d$. This value is close, although smaller, to that shown in Fig. 6.

6 Conclusion

From the above review and numerical study, it appears that numerical simulations of particle transport by two-phase viscous shear flows are now able to reproduce robust features of sediment transport and ripple and dune formation. Results quantitatively agree with those of previous experiments or numerical simulations. In addition, numerical simulations provide measurements which are very difficult to gain from experiments, such as the internal structure of the

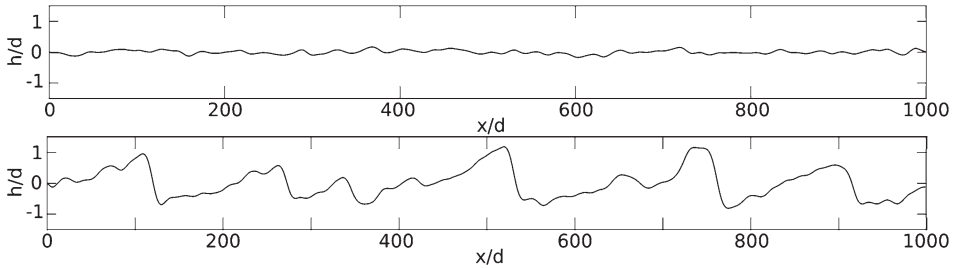

Fig. 6 Bed profile at the initial time $\gamma t = 0$ and $\gamma t = 6000$ (with the mean bed position substracted)

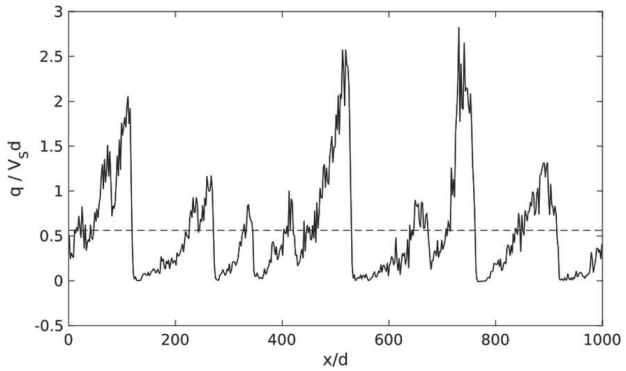

Fig. 7 Dimensionless particle flow rate along the streamwise direction at time $\gamma t = 6000$, for $\theta = 0.4$. *Dashed line*: mean value

bedload layer or the variation of the particle flux along a rippled bed.

Some unanswered questions might therefore receive reliable answers in the near future, and allow for better physical understanding and improvements of the modelling for practical purposes. Among these questions are the fluid stresses on a wavy bed, in either laminar or turbulent flow, and the non-equilibrium response of the particle flux to temporal or spatial variations of the fluid flow. More difficult questions might then be tackled, such as polydisperse or cohesive media, transition from bedload to suspension, or long-term dynamics of granular beds.

Acknowledgements The authors thank Annaig Pedrono for her support in the coupling of the fluid and DEM solvers. The study was supported by the French Agence Nationale de la Recherche (project ANR-12-2013-ModSed), and some of the computational time was provided by the Scientific Grouping CALMIP (project P1027).

Compliance with ethical standards

Conflicts of interest The authors declare that they have no conflict of interest.

References

1. Anderson TB, Jackson R (1967) Fluid mechanical description of fluidized beds. Equations of motion. Ind Eng Chem Fund 6:527–539
2. Aussillous P, Chauchat J, Pailha MMM, Guazzelli E (2013) Investigation of the mobile granular layer in bedload transport by laminar shearing flows. J Fluid Mech 736:594–615
3. Bagnold RA (1956) The flow of cohesionless grains in fluids. Phil Trans R Soc Lond A 249:235–297
4. Bagnold RA (1973) The nature of saltation and of 'bed-load' transport in water. Proc R Soc Lond A 332:473–504
5. Blondeaux P (2001) Mechanics of coastal forms. Annu Rev Fluid Mech 33:339–370
6. Calmet I, Magnaudet J (1997) Large-eddy simulation of high-Schmidt number mass transfer in a turbulent channel flow. Phys Fluids 9:438–455
7. Capecelatro J, Desjardins O (2013) Eulerian-Lagrangian modeling of turbulent liquid-solid slurries in horizontal pipes. Intl J Multiph Flow 55:64–79
8. Charru F, Mouilleron-Arnould H (2002) Instability of a bed of particles sheared by a viscous flow. J Fluid Mech 452:303–323
9. Charru F, Mouilleron H, Eiff O (2004) Erosion and deposition of particles on a bed sheared by a viscous flow. J Fluid Mech 519:55–80
10. Charru F, Andreotti B, Claudin P (2013) Sand ripples and dunes. Annu Rev Fluid Mech 45:469–493
11. Chauchat J, Médale M (2010) A three-dimensional numerical model for incompressible two-phase flow of a granular bed submitted to a laminar shearing flow. Comput Methods Appl Mech Eng 199:439–449
12. Colombini M (2004) Revisiting the linear theory of sand dune formation. J Fluid Mech 502:1–16
13. Colombini M, Stocchino A (2011) Ripple and dune formation in rivers. J Fluid Mech 673:121–131
14. Cundall PA, Strack ODL (1979) A discrete numerical model for granular assemblies. Géotechnique 29:47–65
15. Derksen JJ (2011) Simulations of granular bed erosion due to laminar shear flow near the critical Shields number. Phys Fluids 23(11):1–12
16. Fernandez Luque R, van Beek R (1976) Erosion and transport of bedload sediment. J Hydraul Res 14(2):127–144
17. Fourrière A, Claudin P, Andreotti B (2010) Bedforms in a turbulent stream: formation of ripples by primary linear instability and of dunes by non-linear pattern coarsening. J Fluid Mech 649:287–328
18. Gibilaro LG, Gallucci K, di Felice R, Pagliai P (2007) On the apparent viscosity of a fluidized bed. Chem Eng Sci 62:294–300
19. Houssais M, Ortiz CP, Durian DJ, Jerolmack DJ (2015) Onset of sediment transport is a continuous transition driven by fluid shear and granular creep. Nat Commun 6:6527
20. Izard É, Bonometti T, Lacaze L (2014a) Modelling the dynamics of a sphere approaching and bouncing on a wall in a viscous fluid. J Fluid Mech 747:422–446
21. Izard E, Bonometti T, Lacaze L (2014b) Simulation of an avalanche in a fluid with a soft-sphere/immersed boundary method including a lubrication force. J Comput Multiph Flows 6:391–405
22. Kidanemariam AG, Uhlmann M (2014a) Direct numerical simulation of pattern formation in subaqueous sediment. J Fluid Mech 750:R2
23. Kidanemariam AG, Uhlmann M (2014b) Interface-resolved direct numerical simulation of the erosion of a sediment bed sheared by laminar channel flow. Int J Multiph Flow 67:174–188
24. Lajeunesse E, Malverti L, Charru F (2010) Bedload transport in turbulent flow at the grain scale: experiments and modeling. J Geophys Res 115(F04):001
25. Leighton D, Acrivos A (1986) Viscous resuspension. Chem Eng Sci 41(6):1377–1384

26. Mouilleron H, Charru F, Eiff O (2009) Inside the moving layer of a sheared granular bed. J Fluid Mech 628:229–239
27. Ouriemi M, Aussillous P, Guazzelli E (2009) Sediment dynamics. Part 1. Bed-load transport. J Fluid Mech 636:295–319
28. Raudkivi AJ (2006) Transition from ripples to dunes. J Hydraul Eng 132(12):1316–1320
29. Seminara G (2010) Fluvial sedimentary patterns. Annu Rev Fluid Mech 42:43–66
30. Tenneti S, Garg R, Subramaniam S (2011) Drag law for monodisperse gas-solid systems using particle-resolved direct numerical simulation of flow past fixed assemblies of spheres. Intl J Multiph Flow 37:1072–1092
31. Xiao H, Sun J (2011) Algorithms in a robust hybrid CFD-DEM solver for particle-laden flows. Commun Comput Phys 9(2):297–323
32. Yalin MS (1985) On the determination of ripple geometry. J Hydraul Eng 111:1148–1155